Magnetic/Upconversion Fluorescent $NaGdF_4$:Yb,Er Nanoparticle-Based Dual-Modal Molecular Probes for Imaging Tiny Tumors *in Vivo*

Chunyan Liu,[†] Zhenyu Gao,[‡] Jianfeng Zeng,[†] Yi Hou,[†,*] Fang Fang,[§] Yilin Li,[⊥] Ruirui Qiao,[†] Lin Shen,[⊥] Hao Lei,[§] Wensheng Yang,[‡] and Mingyuan Gao[†,*]

[†]Institute of Chemistry, Chinese Academy of Sciences, Bei Yi Jie 2, Zhong Guan Cun, Beijing 100190, China, [‡]College of Chemistry, Jilin University, Changchun 130012, China, [§]Wuhan Center for Magnetic Resonance, State Key Laboratory of Magnetic Resonance and Atomic and Molecular Physics, Wuhan Institute of Physics & Mathematics, Chinese Academy of Sciences, Wuhan 430071, China, and [⊥]Key Laboratory of Carcinogenesis and Translational Research, Department of Gastrointestinal Oncology, School of Oncology, Peking University, Beijing Cancer Hospital & Institute, Beijing 100142, China

ABSTRACT Detection of early malignant tumors remains clinically difficult; developing ultrasensitive imaging agents is therefore highly demanded. Owing to the unusual magnetic and optical properties associated with f-electrons, rare-earth elements are very suitable for creating functional materials potentially useful for tumor imaging. Nanometer-sized particles offer such a platform with which versatile unique properties of the rare-earth elements can be integrated. Yet the development of rare-earth nanoparticle-based tumor probes suitable for imaging tiny tumors *in vivo* remains difficult, which challenges not only the physical properties of the nanoparticles but also the rationality of the probe design. Here we report new approaches for size control synthesis of magnetic/upconversion fluorescent $NaGdF_4$:Yb,Er nanocrystals and their applications for imaging tiny tumors *in vivo*. By independently varying F^-:Ln^{3+} and Na^+:Ln^{3+} ratios, the size and shape regulation mechanisms were investigated. By replacing the oleic acid ligand with PEG2000 bearing a maleimide group at one end and two phosphate groups at the other end, PEGylated $NaGdF_4$:Yb,Er nanoparticles with optimized size and upconversion fluorescence were obtained. Accordingly, a dual-modality molecular tumor probe was prepared, as a proof of concept, by covalently attaching antitumor antibody to PEGylated $NaGdF_4$:Yb,Er nanoparticles through a "click" reaction. Systematic investigations on tumor detections, through magnetic resonance imaging and upconversion fluorescence imaging, were carried out to image intraperitoneal tumors and subcutaneous tumors *in vivo*. Owing to the excellent properties of the molecular probes, tumors smaller than 2 mm was successfully imaged *in vivo*. In addition, pharmacokinetic studies on differently sized particles were performed to disclose the particle size dependent biodistributions and elimination pathways.

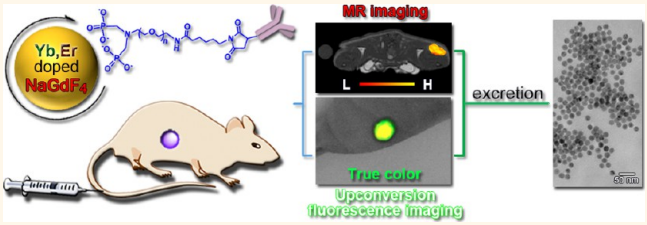

KEYWORDS: magnetic/upconversion fluorescent nanoparticles · dual-modal molecular probes · *in vivo* tumor imaging · tiny tumor · pharmacokinetics

Imaging techniques used for cancer diagnosis and research including X-ray computed tomography (CT), magnetic resonance imaging (MRI), positron emission tomography (PET), single photon emission CT (SPECT), ultrasound, and versatile optical imaging technologies, though remaining at preclinical stages, present different strengths and limitations as well,[1−11] depending on the imaging principle for deriving the visual information. Among them, MRI is considered to be superior for acquiring high spatial resolution anatomical and physiological images, while the optical imaging techniques show a clear trend for translation into the clinic due to the high imaging sensitivity and low cost of the imaging facilities. In this context, multifunctional molecular probes offer possibilities to combine different imaging modalities for improving the diagnostic efficacy of early malignant tumors.

Owing to the unusual magnetic and optical properties associated with f-electrons, rare-earth (RE) elements are very suitable for creating multifunctional materials, while nanoparticles provide such an ideal platform that the unique magnetic and upconversion

* Address correspondence to gaomy@iccas.ac.cn, houyi@iccas.ac.cn.

Received for review May 26, 2013 and accepted July 23, 2013.

Published online July 23, 2013
10.1021/nn4030898

fluorescent properties can be integrated within single particles upon proper choices of particle matrix and dopants. $NaREF_4$ particles have been demonstrated to be a suitable matrix apart from their potential as an MRI contrast agent,[12,13] while Yb^{3+}/Er^{3+} doping can give rise to upconversion fluorescence that locates at shorter wavelength with respect to excitation.[14−18] In comparison with the conventional fluorescent nanoparticles, the upconversion fluorescent counterparts are favorable for *in vivo* imaging, as near-infrared excitation can better penetrate tissue than visible light while giving rise to greatly reduced background noise.[14,15,19,20] Most importantly, green emission that can be obtained by proper control over the crystalline phase of $NaREF_4$:Yb,Er nanocrystals[21,22] is potentially useful for surgical navigation because it is sensitive not only to the naked eye but also to Si-based optical detectors.

Nevertheless, the applications of RE-based nanocrystals for *in vivo* imaging of tiny tumors, defined herein as tumors of 1−4 mm, first challenge the synthetic method for achieving nanocrystals with well-defined structures and properly balanced physical properties.

So far, different synthetic approaches based on coprecipitation,[23,24] hydro(solvo)thermal synthesis,[19,25] thermal decomposition of organic precursors,[20,26,27] and replacement reactions[12,13,28,29] have been developed for synthesizing versatile RE-based nanocrystals. High-temperature approaches generally favor inorganic nanocrystals with high crystallinity degree and narrow size distribution, irrespective of the type of nanocrystal.[30,31] However, hydro(solvo)thermal synthesis is faced with technical difficulties in monitoring the particle growth over time. Although the thermal decompositions of organic precursors such as $Na(CF_3COO)$ and $RE(CF_3COO)_3$ have been proven to be effective in achieving rare-earth nanocrystals with narrow size distributions,[20] the ratios among the components of the desired nanocrystals are restricted by the precursors, which may limit the room for largely tuning the morphology of the desired nanocrystals.

In contrast, the synthetic route for replacement reactions taking place at high temperature, pioneered by Zhang as a user-friendly approach,[29] offers much more room and flexibility for tuning the morphology and optical properties of RE-based nanocrystals. The temperature allowing for the nucleation process, typically below 100 °C, was found to be effective for achieving $NaYF_4$ nanocrystals of different shapes.[32] The time duration of the nucleation process was also used to tune the size of monodispersed $NaGdF_4$ nanocrystals, but in a narrow size regime of 2.5−8.0 nm.[13] The reaction temperature for particle growth, typically above 250 °C, is however more effective for regulating the size of the resultant nanocrystals.[33] Apart from the nucleation temperature and particle growth temperature, the ratio of the solvent and surface capping agent is also an effective variable but more favorable for achieving nonspherical nanocrystals of different sizes.[29,34,35]

In spite of the remarkable progress mentioned above in morphology control, the particle size variation was found to be accompanied by different crystalline phases, which are strongly associated with the upconversion fluorescence.[33,34] In addition, RE-based nanocrystals with excellent monodispersity and effective particle size tunability lack systematic studies, especially in the size regime of 5−50 nm, which are essentially demanded for tumor imaging applications. In other words, the synthetic approach is awaiting further optimization especially for preparing magnetic/upconversion fluorescent nanocrystals with appropriate size, narrow particle size distribution, and properly balanced optical emissions.

Second, the applications of RE-based nanocrystals for *in vivo* imaging of tiny tumors also challenge the rationality of probe design including biocompatible surface engineering and surface biofunctionalization.

Li and co-workers have performed a series of research works on *in vivo* applications of RE-based nanoparticles, including multimodality *in vivo* imaging of non-tumor-bearing mice,[18,36,37] *in vivo* tumor-targeted upconversion fluorescence imaging,[38] and long-term biodistribution of upconversion fluorescent nanoparticles.[39] Through the enhanced permeability and retention (EPR) effect, Hyeon and co-workers reported *in vivo* imaging of tumors upon the use of magnetic/upconversion fluorescent nanorods of 33 × 44 nm formed by coating $NaYF_4$:Yb,Er nanocyrstals with $NaGdF_4$.[40] Other researchers performed MRI and upconversion fluorescence imaging of tumors *via* intratumoral injection of the nanoparticles,[41,42] showing that the nanoparticles preserved their magnetic/upconversion fluorescent properties in tumor microenvironments. By summarizing the above-mentioned investigations, it can be found that the tumors visualized upon fluorescence imaging and/or MRI, irrespective of the targeting mechanisms, particle size and shapes, surface coating, *etc.*, are around 5 mm[12,38,43,44] or in a size range of 10−20 mm,[41,42,45] quite comparable to the imaging results achieved by using magnetic iron oxide nanoparticles.[18,46,47] Nevertheless, more sensitive *in vivo* imaging is reasonably expected since RE-based nanocrystals possess superior magnetic and optical properties.

Assuming that tumors are spherical, the volume is proportional to the third power of the tumor radius. The order of magnitude roughly remains even if tumors often take different shapes.[48] Accompanying the sharp reduction in volume, the mean vessel size dramatically decreases against tumor size in the range of 2−10 mm.[49] According to previous studies, although the uptake of macromolecular drugs in small tumors per mass is higher than that in large tumors,

the absolute uptake is lower for small tumors due to the greatly reduced size.[50,51] Moreover, in spite of the poorly aligned and leaky structure of vessels, previous tumor perfusion studies revealed that small tumors have comparable geometric resistances to normal tissues, while large tumors have higher geometric resistance, and this size-dependent geometric resistance becomes very dramatic for tumors smaller than 15 mm.[52] Therefore, it is reasonable to infer that it is more difficult for nanoparticles to be trapped in small tumors due to higher blood flow rate, which is probably the reason that most imaging results achieved so far based on nanoprobes were on tumors of 5−15 mm. In this context, *in vivo* imaging of tiny tumors as defined herein challenges not only the advanced physical properties of the probes but also the rationality of probe design.

On the basis of our previous investigations on *in vivo* tumor imaging,[8,12,53] herein we report our recent results on the controlled synthesis of magnetic/upconversion fluorescent $NaGdF_4$:Yb,Er nanocrystals, construction of dual-modality molecular probes, active targeting of tumors for MRI and optical imaging, and particle size-dependent pharmacokinetic behaviors, with immense efforts to disclose the potential of RE-based nanocrystals for imaging tiny tumors *in vivo*. In addition, the mechanisms for regulating the particle size and shapes of $NaGdF_4$:Yb,Er nanocrystals were investigated and discussed.

RESULTS AND DISCUSSION

Preparation of $NaGdF_4$:Yb,Er Nanocrystals. As mentioned in the Experimental Section, the high-temperature replacement reactions among $LnCl_3$ (Gd, Yb, and Er), NH_4F, and NaOH were adopted for synthesizing $NaGdF_4$:Yb,Er nanocrystals, and oleic acid (OA) was chosen as both particle surface capping agent and cosolvent used together with 1-octadecene. Figure 1 presents the evolutions of particle size, phase structure, and upconversion fluorescence against reaction time at 300 °C. In fact, as shown in Figure S1 in the Supporting Information (SI), tiny nuclei were formed during the nucleation process at 50 °C. Then, the particle size was slightly increased to ~2.1 nm right after the temperature of the reaction mixture reached 300 °C, as shown in Figure 1a. These particles are in cubic phase, as indicated by electron diffraction analysis shown in the inset of Figure 1a. The initial 10 min of reaction leads to a faster growth of a certain percentage of the particles, which greatly broadens the particle size distribution, as shown in Figure 1b. In the meantime, particles, probably the large ones, occur in hexagonal phase with most particles remaining in cubic phase, supported by the assignments of electron diffraction patterns shown in the inset of Figure 1b. Further prolonging the reaction time to 20 min quickly increases the particles size and completely changes the

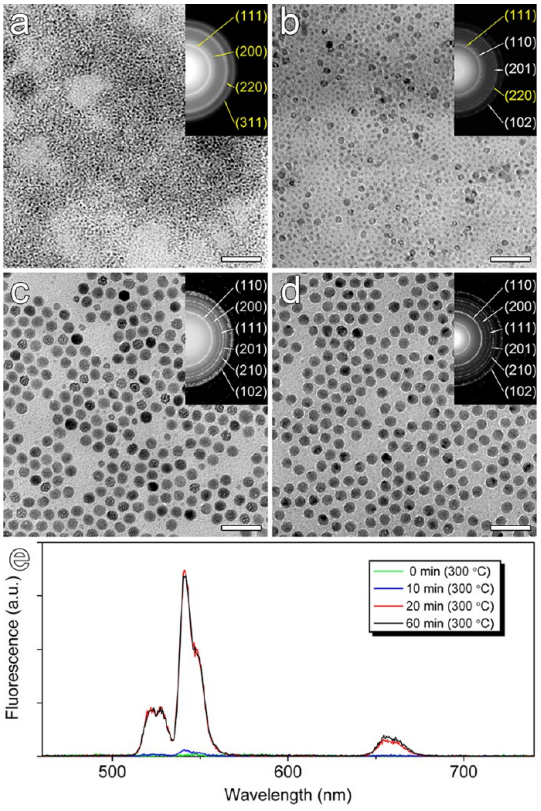

Figure 1. Transmission electron microscopy (TEM) images of $NaGdF_4$:Yb,Er nanoparticles obtained at 300 °C at different reaction times, *i.e.*, 0 min (a), 10 min (b), 20 min (c), and 60 min (d). The scale bars embedded in the TEM images correspond to 50 nm. The insets are electron diffraction patterns overlaid with the identifications of different diffraction rings labeled with Miller indices of cubic (yellow) and hexagonal $NaGdF_4$ (white) according to JCPDS cards (Nos. 27-0697 and 27-0699). Frame e shows the upconversion fluorescence spectra of different $NaGdF_4$:Yb,Er nanoparticles recorded upon excitation by a CW 980 nm laser.

crystalline phase from cubic to hexagonal, as shown in the inset of Figure 1c, but a certain percentage of small particles of 5−6 nm remain in the system. However, due to Ostwald ripening, these small particles disappear when the reaction time is prolonged to 60 min. Consequently monodispersed particles of ~14 nm are obtained, as shown in Figure 1d. In combination with the upconversion fluorescence results presented in Figure 1e, it can be concluded that small nanoparticles in cubic phase do not exhibit upconversion fluorescence, contrasting with large nanoparticles in hexagonal phase. Moreover, the intensity of upconversion fluorescence remains nearly unchanged if comparing the particles obtained at 20 and 60 min, respectively, suggesting that the upconversion fluorescence is relatively independent of the particle size distribution. Nevertheless, the prolonged reaction time quite obviously favors the formation of monodispersed nanoparticles, although the reaction time at 300 °C is not very effective for tuning the size of $NaGdF_4$:Yb,Er nanocrystals in hexagonal phase. Further inductively coupled plasma atomic emission spectrometer

(ICP-AES) measurements reveal that the ratio of Gd:Yb:Er in the nanocrystals shown in Figure 1d is 79.6:18.3:2.1.

Impacts of F^-:Ln^{3+} Ratio on $NaGdF_4$:Yb,Er Nanocrystals. The reaction temperature for particle growth, typically above 250 °C, was previously used to tune the size of $NaYF_4$:Yb,Er nanocrystals from 5 to 40 nm, but the shape of the resultant nanocrystals was simultaneously altered. Moreover, the size distribution of the spherical particles remained broad.[34] Therefore, in the current investigations, we explored the impacts of other experimental variables so as to obtain monodispersed $NaGdF_4$:Yb,Er nanocrystals of different sizes. In this context, the preparation was designed such that each component in the desired $NaGdF_4$:Yb,Er nanocrystals was supplied by independent reactants, *i.e.*, $LnCl_3$ (Gd, Yb, and Er), NH_4F, and NaOH, which allowed disclosing the impacts of major reactant ratios such as F^-:Ln^{3+} and Na^+:Ln^{3+} on the size, size distribution, and crystalline phase structure of the resultant nanocrystals. It should be mentioned that in the following preparations all synthetic parameters were kept unchanged except for the inspecting variables.

A series of preparations were first carried out by varying the F^-:Ln^{3+} ratio while fixing the Na^+:Ln^{3+} ratio at 2.5:1. Figure 2 presents the nanocrystals obtained by different F^-:Ln^{3+} ratios, *i.e.*, 8:1 (Figure 2a), 4:1 (Figure 2b), 3.2:1 (Figure 2c), and 2.4:1 (Figure 2d). As shown in Figure 2a, the ratio of 8:1 leads to polydispersed $NaGdF_4$:Yb,Er particles with bigger ones tending to grow into nanorods and small ones of 8−25 nm being prone to form faceted particles. The formation of faceted particles suggests that the energies of crystal edges and corners are effectively reduced due to the high surface coverage of F^- ions;[54] the broadened size distribution however implies that repetition nucleation takes place if the F^-:Ln^{3+} ratio is much higher than the stoichiometric ratio in $NaGdF_4$:Yb,Er. However, the formation of monodispersed spherical $NaGdF_4$:Yb,Er particles of 14.6 ± 0.7 nm, as shown in Figure 2b, suggests that the repetition nucleation is dramatically suppressed when the feeding F^-:Ln^{3+} ratio is close to that in the desired nanocrystals, *i.e.*, 4:1. High-resolution TEM (HRTEM) analysis shown in Figure S2a in the SI suggests that the resultant nanoparticles are hexagonal-phase single crystals, which is positively supported by the powder X-ray diffraction (XRD) analysis shown in Figure S2b. Further decreasing the F^-:Ln^{3+} ratio to 3.2:1 significantly increases the particle size to 24.6 ± 1.1 nm and in the meantime slightly compresses the resultant particles, as shown in Figure 2c. These tendencies persist when the F^-:Ln^{3+} ratio is decreased to 2.4:1. Consequently, wheel-shaped $NaGdF_4$:Yb,Er nanoparticles of 36.7 ± 2.4 nm are formed (Figure 2d). According to the HRTEM analysis shown in the inset of Figure 2d, the transformation of particle shapes can be understood as

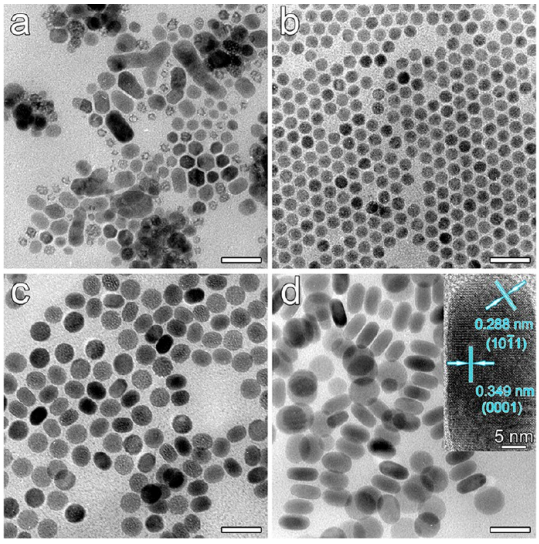

Figure 2. TEM images of $NaGdF_4$:Yb,Er nanoparticles prepared at 300 °C by different F^-:Ln^{3+} feeding ratios, *i.e.*, 8:1 (a), 4: 1 (b), 3.2:1 (c), and 2.4:1 (d). The scale bars embedded correspond to 50 nm. The inset in frame d is an HRTEM image of a selected wheel-shaped particle overlaid with the identifications of crystal planes according to hexagonal $NaGdF_4$ (JCPDS No. 27-0699).

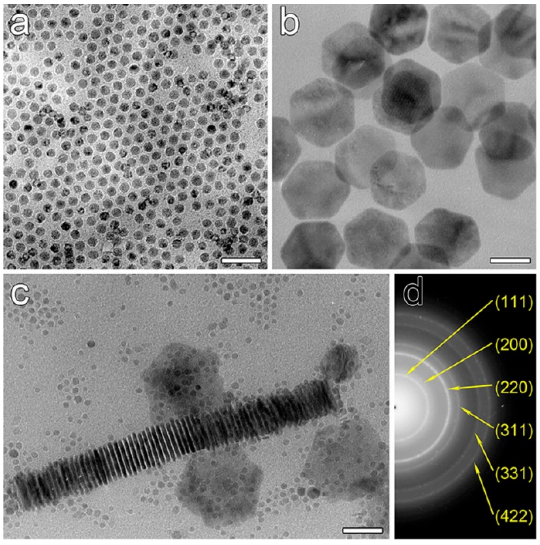

Figure 3. TEM images of $NaGdF_4$:Yb,Er nanoparticles prepared at 300 °C by different Na^+:Ln^{3+} feeding ratios, *i.e.*, 3:1 (a), 1.5:1 (b), and 0.75:1 (c). The scale bars embedded correspond to 50 nm. Frame d is the electron diffraction pattern of the small particles shown in frame c overlaid with identifications of different diffraction rings labeled with Miller indices of cubic $NaGdF_4$ (JCPDS No. 27-0697).

follows. Decreasing the F^-:Ln^{3+} ratio will reduce the number of F^- ions capping the particle surface, as OA prefers to attach to the (0001) surface of $NaLnF_4$ nanocrystals.[20,25] The growth of the particles along the [0001] direction is therefore prohibited, leading to the formation of compressed spherical particles.

Careful comparison reveals that the relative size distribution is actually decreased from 4.8% for 14.6 nm particles to 4.5% for 24.6 nm particles and

then slightly increased to 6.5% for 36.7 nm ones. The small variation in the relative size distribution against particle size implies that there is nearly no repetition nucleation occurring when reducing the F^-:Ln^{3+} ratio from 4:1 to 2.4:1, which favors the formation of monodispersed $NaGdF_4$:Yb,Er nanocrystals.

Impacts of Na^+:Ln^{3+} Ratio on $NaGdF_4$:Yb,Er Nanocrystals. As shown in Figure 3, increasing the Na^+:Ln^{3+} ratio from 2.5:1 (Figure 2b) to 3:1 effectively decreases the particle size from 14.6 ± 0.7 nm to 11.5 ± 0.7 nm (Figure 3a) without altering the spherical shape and crystalline phase of the resultant $NaGdF_4$:Yb,Er nanocrystals (Figure S3a). In huge contrast, decreasing the Na^+:Ln^{3+} ratio to 1.5:1 directly leads to the formation of hexagonal-phase nanosheets of 82.3 ± 4.1 nm (Figure 3b), while further decreasing the Na^+:Ln^{3+} ratio to 0.75:1 results in the coexistence of both hexagonal nanosheets of 49.5 ± 3.3 nm and small particles of 6.2 ± 1.0 nm, as shown in Figure 3c. Electron diffraction analysis reveals that the large nanosheets are in hexagonal phase (Figure S3b), while the small particles are in cubic phase (Figure 3d).

On one hand, raising the Na^+:Ln^{3+} ratio increases the overall concentrations of cationic ions for forming the desired particles, which in consequence reduces the size of the resultant nanoparticles. On the other hand, excessive Na^+ ions in the system reduces the surface coverage of Ln^{3+} and diminishes the impact of the OA ligand on shape regulation. On the contrary, reducing the Na^+:Ln^{3+} ratio increases the surface coverage of Ln^{3+} ions. Since the OA ligand binds firmly to Ln^{3+} rather than Na^+, the growth along the [0001] direction is heavily prohibited, as the (0001) surfaces are rich in Ln^{3+}; consequently, heavily compressed nanocrystals (*i.e.*, nanosheets) rather than slightly compressed spherical particles are formed. The formation of small cubic-phase particles can be explained by the fact that Ln^{3+} (Gd^{3+}, Yb^{3+}, and Er^{3+}) and Na^+ occupy the relatively fixed cationic sites in hexagonal-phase $NaGdF_4$:Yb,Er, while they are randomly distributed within the cationic sublattice in cubic-phase $NaGdF_4$:Yb,Er.[22,55] Thus, the transformation of small particles from cubic phase to hexagonal phase is suppressed when the amount of Na^+ ion is greatly reduced in the system.

To briefly summarize the above experimental results, with reference to the stoichiometric ratio of Na^+:Ln^{3+}:F^- in $NaGdF_4$:Yb,Er, decreasing the F^-:Ln^{3+} ratio or increasing the Na^+:Ln^{3+} ratio favors the formation of monodispersed $NaGdF_4$:Yb,Er nanocrystals in spherical or quasi-spherical shapes. Conversely, increasing the F^-:Ln^{3+} ratio encourages repetition nucleation, resulting in a broadened size distribution, while decreasing the Na^+:Ln^{3+} ratio leads to $NaGdF_4$:Yb,Er nanosheets instead of spherical nanocrystals.

Impacts of $NaGdF_4$:Yb,Er Nanocrystal Size on Optical Properties. Owing to the excellent size uniformity, nanocrystals of 11.5 ± 0.7 (Figure 3a), 14.6 ± 0.7 nm (Figure 2b), 24.6 ± 1.1 nm (Figure 2c), and 36.7 ± 2.4 nm (Figure 2d), named sample a, sample b, sample c, and sample d, respectively, were adopted to further show the particle size dependent upconversion fluorescence. Figure 4 presents upconversion fluorescence spectra of samples a–d normalized with respect to Ln^{3+} concentration. Three major emissions located at 521, 541, and 655 nm, independent of particle size, were recorded. They can be attributed to radiative relaxations from $^2H_{11/2}$, $^4S_{3/2}$, and $^4F_{9/2}$ states to the $^4I_{15/2}$ state of Er^{3+}, respectively, achieved *via* complicated energy transferring processes between Yb^{3+} and Er^{3+}, and the absorption of the second photon of 980 nm laser light by Er^{3+}.

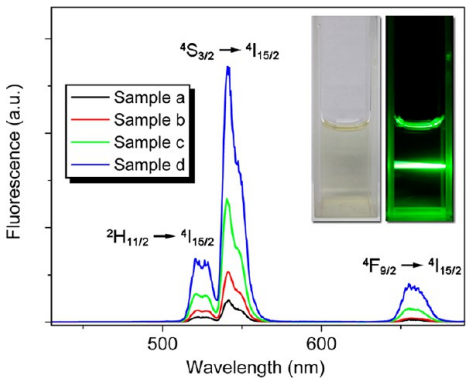

Figure 4. Normalized fluorescence spectra of sample a, sample b, sample c, and sample d, recorded upon excitation by a CW 980 nm laser. The insets are photographs of a cyclohexane solution of sample c taken under ambient light (left) or in the dark under excitation by a 980 nm laser (right).

TABLE 1. Integrated Upconversion Fluorescence Emission and the Green to Red Emission Ratio ($ratio_{G/R}$) of Monodispersed $NaGdF_4$:Yb,Er Nanocrystals of Different Sizes

sample	size (nm)	total emission	green emission	red emission	$ratio_{G/R}$
a	11.5	2423	2126	237	8.9
b	14.6	5482	4956	440	11.3
c	24.6	13653	12013	1498	8.0
d	36.7	30088	25742	4051	6.4

In brief, the overall integrated upconversion fluorescent emission increases with the particle size, which is because a decreased specific surface area is favorable for reducing the nonradiative relaxation pathways.[56] In contrast, the green-to-red emission ratio presents roughly an opposite tendency when the particle size is higher than 14 nm, as shown in Table 1, which can be interpreted by the fact that the nonradiative decay that mainly quenches the green emission is enhanced in larger particles due to the higher surface density of OA ligands,[22,28,29] since the larger particles are obtained by reduced F^-:Ln^{3+} ratios.

In fact, the particles of 10–100 nm are believed to be suitable for *in vivo* imaging of tumors, based on

previous investigations on different types of inorganic nanoparticles and comprehensive studies on macromolecular antitumor drugs as well.[57,58] The bottom limit in principle is set according to renal clearance so as to gain a long enough blood half-time to enhance the tumor accumulation of a given nanoprobe. The top limit is not only dictated by the pore size (>100 nm) of the leaky tumor vasculatures but also strongly associated with the uptake by the mononuclear phagocyte system (MPS), which leads to different biodistribution patterns. As MPS uptake is very complicated, depending on both the size and solution properties of nanoparticles, the upper limit is also viewed differently. Although the monodispersed particles (samples a−d) generally meet the size requirement for *in vivo* tumor imaging, by taking the overall upconversion fluorescence intensity and green-to-red emission ratio, sample c was selected for the following experiments. Under 980 nm laser excitation, sample c particles dispersed in cyclohexane present very bright green emission, as shown in the inset of Figure 4.

Characterizations of PEGylated $NaGdF_4$:Yb,Er Nanoparticles. With respect to tumor probe construction, colloidal stability of given nanoparticles under physiological conditions is essentially required for achieving long blood circulation time, as the particle agglomeration will enhance MPS uptake of the particles and greatly reduce their plasma residence time. The *in vivo* applications of RE-based nanocrystals especially for tumor imaging, from our point of view, still lack effective surface engineering chemistry in comparison with superparamagnetic counterparts, *i.e.*, magnetic iron oxide nanoparticles,[53,59−62] although different efforts have been devoted so far.[18,63−65]

Following on from our previous investigations,[12] a bifunctional ligand, PEG2000 bearing a maleimide group at one end and two phosphate groups at the other end (mal-PEG-dp), was designed and used to replace the oleate ligand to render the oleate-coated $NaGdF_4$:Yb,Er nanocrystals water-soluble and provide surface reactive groups for further constructing $NaGdF_4$:Yb,Er-based tumor imaging probes. The colloidal stability in different aqueous media and the optical stability with respect to upconversion fluorescence emissions of the resultant PEGylated $NaGdF_4$:Yb,Er particles were carefully characterized. As shown in Figure 5a, the PEGylated particles present excellent colloidal stability not only in Milli-Q water but also in PBS buffer, which is highly essential for further exploring *in vivo* applications of the underlying nanocrystals. Moreover, the PEGylated particles also present superstable optical emissions at both 541 and 655 nm (Figure 5b) in water and PBS buffer, respectively, although the emission intensity and the green-to-red emission ratio are decreased after the particles are transferred into water, as shown in Figure S4 in the SI.

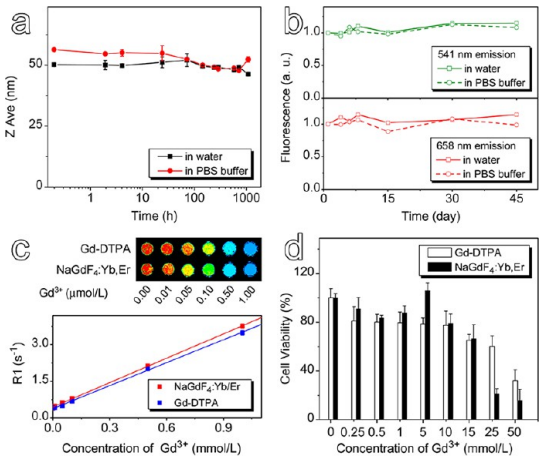

Figure 5. (a) Temporal evolutions of the hydrodynamic size of (mal-PEG-mp)-coated $NaGdF_4$:Yb,Er nanoparticles in water and PBS buffer, respectively. (b) Temporal evolutions of the upconversion fluorescence emissions at 541 and 655 nm recorded from the nanoparticles in water and PBS buffer, respectively. (c) Color-coded T1-weighted MR images of aqueous solutions of PEGylated $NaGdF_4$:Yb,Er nanoparticles and Gd-DTPA with different Gd concentrations in 2 mL Eppendorf tubes (top panel) and experimental data (solid square points) together with the corresponding theoretical fittings (solid lines) of the relaxation rate R1 (bottom panel). (d) Viability of GC7901 cells recorded after being incubated with PEGylated $NaGdF_4$:Yb,Er nanoparticles or Gd-DTPA with different Gd^{3+} concentrations.

The MRI contrast enhancement effect of the PEGylated $NaGdF_4$:Yb,Er nanoparticles is shown in Figure 5c. By linear regression fitting of the experimental data, the molar relaxivity r1 is extracted to be 3.33 mM^{-1} s^{-1}, slightly higher than that (3.19 mM^{-1} s^{-1}) for Gd-DTPA (Magnevist).

The cell viability data obtained *via* the methyl thiazolyl tetrazolium (MTT) assays are shown in Figure 5d. In comparison with Gd-DTPA, the PEGylated $NaGdF_4$:Yb,Er nanoparticles present comparable cell viabilities at Gd^{3+} concentrations below 10 mmol/L, which is much higher than the clinical dose for Gd-DTPA (0.3 mmol/kg body weight), but dramatically increased toxicity if the Gd^{3+} concentration is increased to 25 mmol/L.

MR Imaging of Tumors *in Vivo*. Nanoparticles with proper size have been demonstrated to be capable of targeting tumors by taking advantage of the leaky vasculature of tumors, known as passive tumor targeting.[66] To further increase the tumor accumulation of given nanoprobes, various types of tumor-specific bioligands were used to enhance the binding affinity of the particles to tumors, leading to active tumor targeting.[57,66] The epidermal growth factor receptor (EGFR) has been demonstrated to be a rational target of anticancer therapy. Herein, to achieve tumor-specific targeting ability, a commercially available monoclonal anti-EGFR antibody (mAb, Erbitu) used as a clinical drug for the treatment of colorectal cancers was covalently conjugated to the

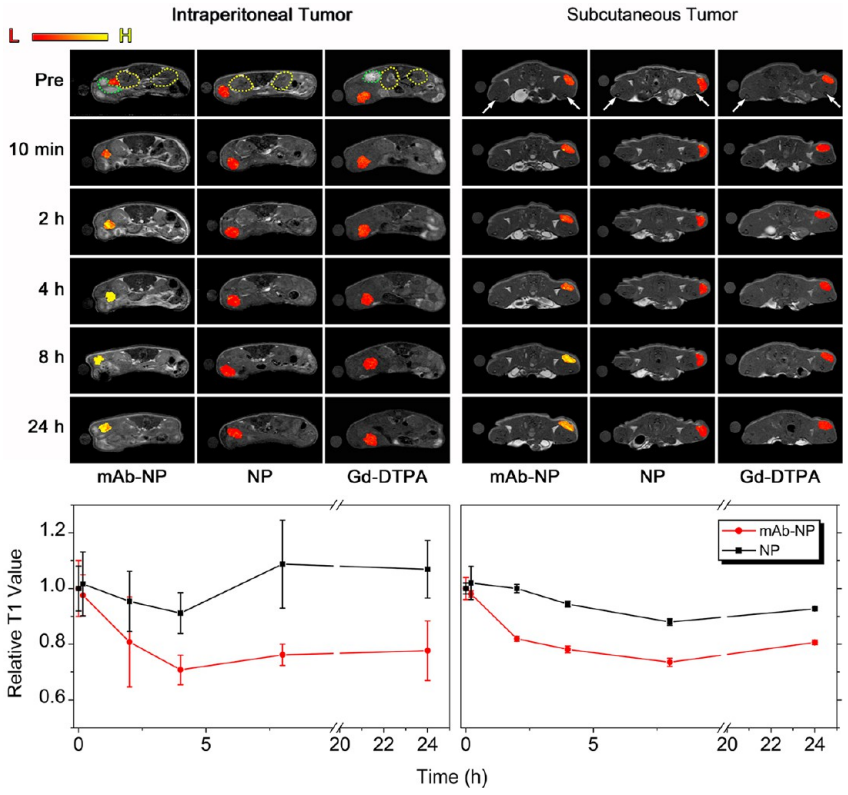

Figure 6. Top panel: T1-weighted MR images acquired before and at different time points after intravenously injecting mAb-NP probe, mother particle (NP), and Gd-DTPA into mice bearing intraperitoneally (left) and subcutaneously (right) transplanted tumors, respectively. The tumor sites are color-coded to better show the contrast enhancing effects, and organs such as kidney (encircled by yellow dotted line), stomach (encircled by green dotted line), and tibia (indicated by white arrows) are identified. Bottom panel: T1 values of the tumor sites extracted before and after injections of the aforementioned imaging agents.

(mal-PEG-dp)-coated $NaGdF_4$:Yb,Er nanoparticles through "click" reaction. The conjugation reaction and the formation of the conjugates were investigated by fluorescence spectroscopy and dynamic light scattering (DLS). The fluorescence spectroscopy studies, as shown in Figure S5 in the SI, demonstrate that the yield of the "click" reaction approaches 95%. Thus, the average number of mAb molecules on each $NaGdF_4$:Yb,Er nanoparticle is estimated to be ~3.8, which is supported by the reasonable increment in the hydrodynamic size of the resultant particles (Figure S6). The DLS analysis shown in the SI further demonstrates that no particle coagulation occurs as a consequence of the conjugation reaction, suggesting that the bioconjugation reaction takes place in a well-controlled manner.

With respect to *in vivo* tumor imaging, both intraperitoneally and subcutaneously xenografted tumors were constructed. The intraperitoneal tumor model can better reflect the nature of cancers, as it can be taken as a metastatic model, while the subcutaneous tumor model offers a better opportunity to visualize the tumor through optical imaging.

Through the tail vein, the particle probe (mAb-NP) obtained as mentioned above was injected into BALB/c nude mice bearing LS180 tumor xenografts. The mother particles (NP) and Gd-DTPA were set as negative controls and used at the same dose level with respect to Gd concentration. T1-weighted MR images acquired before and at different time points postinjection are provided in the upper panel of Figure 6. In comparison with Gd-DTPA, the mother particle can slightly enhance the contrast of the tumor region, probably caused by the enhanced permeability and retention of particles in tumor. However, the MR contrast enhancement is greatly increased by the mAb-NP probe with respect to both tumor models, characterized by strongly shortened T1 values of the tumor regions, as shown in the bottom panel of Figure 6. The maximum $\Delta T1$ achieved from the intraperitoneal and subcutaneous tumors is around 30% (4 h postinjection) and 27% (8 h postinjection), respectively, contrasting with 9% and 12% induced by the mother particle. The time difference for reaching the maximum $\Delta T1$ is probably caused by the differences between the microenvironments and blood supplies of the intraperitoneal and subcutaneous tumors.

Upconversion Fluorescence Imaging of Tumors *in Vivo*. With respect to optical imaging of tumors *in vivo*, the subcutaneous tumor model was adopted to better show the tumor-specific targeting and imaging effects. The mAb-NP probe was injected into nude mice bearing tumors at the flank region of the right hind leg

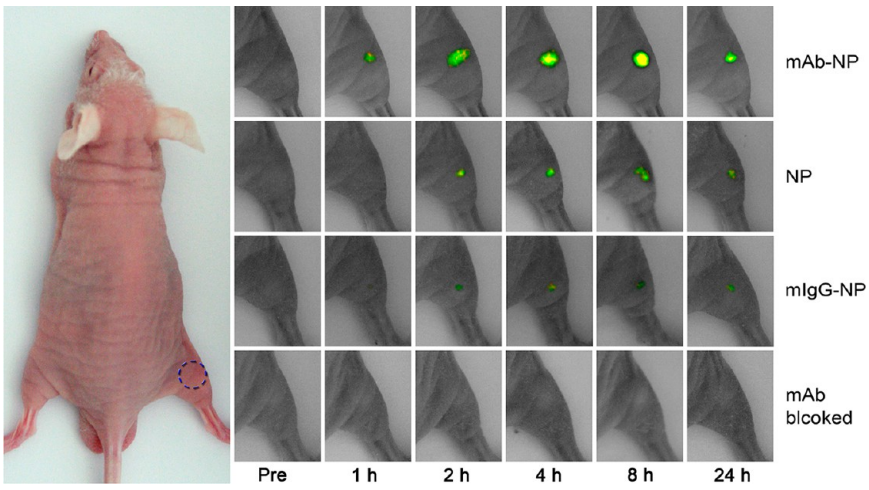

Figure 7. Left panel: Optical image of a nude mouse overlaid with a blue dashed circle indicating the 980 nm laser beam size, which can fully cover the xenografted tumors. Right panel: Four sets of bright-field optical images of the tumor region overlaid with true-color upconversion fluorescence images recorded before and at different time points after intravenous injection of mAb-NP, NP, and mIgG-NP, respectively. The images captured in the cold mAb experiment are labeled "mAb blocked" and placed in the last row.

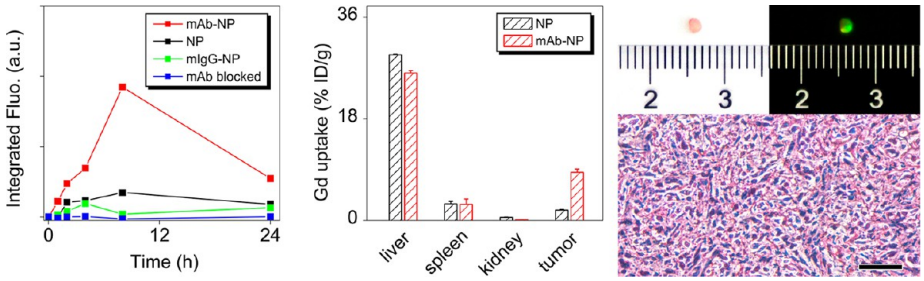

Figure 8. Left frame: Temporal evolutions of the integrated upconversion fluorescence signals extracted from the tumor images shown in the right panel of Figure 7. Middle frame: Biodistributions of mAb-NP probe and the mother particle (NP) in tumor and main organs of mice determined at 24 h postinjection. Right frame: True-color optical images of a freshly harvested tumor (top) together with an H&E staining image of a tissue slice from the tumor shown above (bottom). The scale bar corresponds to 50 μm.

through the tail vein. The dosage level was set the same as that for MRI experiments. The mother particle and a reference probe (mIgG-NP) were adopted as negative controls. In addition, a cold mAb experiment was also carried out by injecting mAb 4 h prior to the injection of the mAb-NP probe.

A set of true-color upconversion fluorescence images taken at different time points postinjection is presented in the right panel of Figure 7. A significant green fluorescence appears 60 min after the injection of the mAb-NP probe, and this green emission increases in intensity and reaches a maximum at 8 h postinjection, followed by decay upon prolonged observation, which is rather in consistence with the MRI results. Similar to the mAb-NP probe, the mother particle and the mIgG-NP probe also present similar signal evolution tendencies, but the fluorescence signals are much weaker, which can be interpreted by limited tumor uptake of the mother particle or mIgG-NP through the EPR effect. In huge contrast, the mAb-NP gives rise to nearly no fluorescence signal from the tumor region in the mAb blocked experiment. It is at present not very clear why the tumor uptake through the EPR effect was further suppressed when cold antibody was administrated prior to the mAb-NP probe, which is probably because the specific binding of excessive cold antibody to tumors reduces the permeability of blood vessels therein. More quantitative analyses on the fluorescence signals recorded after the injections of the particle probes and the control particles, respectively, are provided in the left frame of Figure 8. To further verify the difference in tumor uptakes of the mAb-NP probe and the mother particles, the tumors together with important organs such as liver, spleen, and kidney were harvested 24 h postinjection to determine their Gd concentrations. As shown in the middle frame of Figure 8, the tumor uptake of the mAb-NP probe is increased by a factor of 4.6, in comparison with the mother particle, which is in very good agreement with the optical imaging results. Nevertheless, the liver uptake dominates the biodistribution of the particle probes and the mother particles at least at 24 h postinjection. In addition, spleen also presents some uptake but at lower levels.

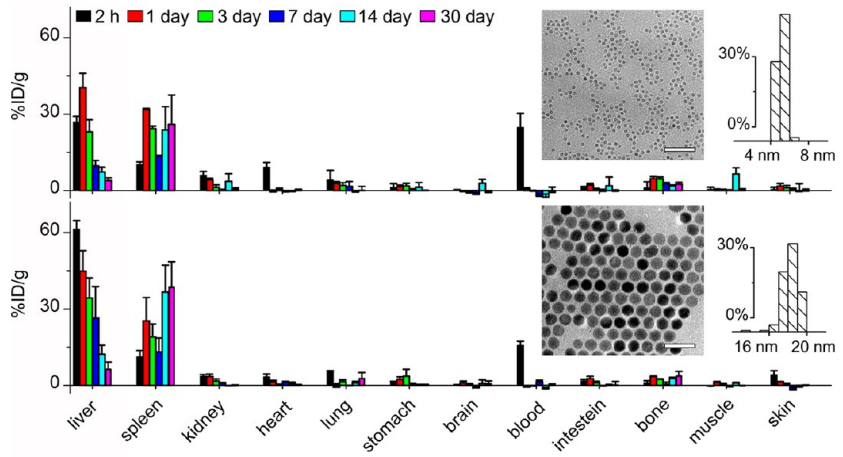

Figure 9. Biodistribution of 5.1 nm ($NaGdF_4$) and 18.5 nm ($NaGdF_4$:Yb,Er) nanoparticles in different organs and tissues of mice. The TEM images and particle size histograms of these two nanoparticle samples are provided as insets. The scale bars embedded in the TEM images correspond to 50 nm.

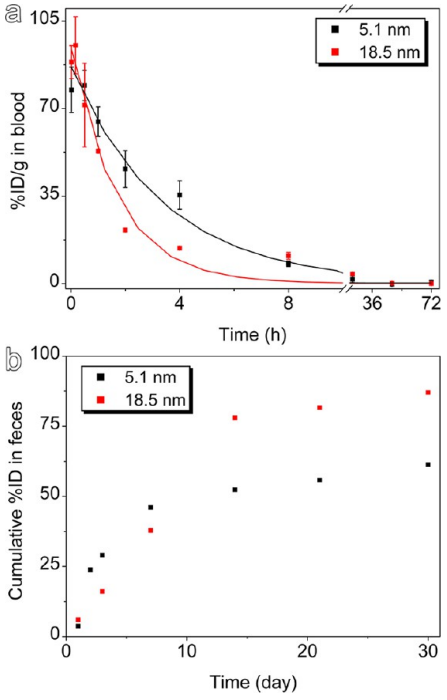

Figure 10. (a) Blood clearance profiles of 5.1 and 18.5 nm particles in Kunming mice (n = 4). The solid lines are theoretical fitting curves depicting the clearance behaviors based on the single-compartment model. (b) Cumulative amounts of 5.1 and 18.5 nm nanoparticles found in feces of mice at different time points postinjection (n = 8).

A bright-field image and a dark-field fluorescence image of a freshly harvested solid tumor of 1.7 mm × 1.9 mm are presented in the right frame of Figure 8. The fluorescence tumor image coincides well with the bright-field tumor image. Further histopathological analysis on the excised tumor tissue was carried out upon hematoxylin and eosin (H&E) staining. As shown in the bottom image in the same frame, the cells become polygonal and elongated with a dramatically increased nucleus-to-cytoplasm ratio being present in comparison with normal tissue cells while the interstitial tissue develops, suggesting that the tissue shown in the upper images can be identified as solid tumor formed by the transplanted tumor cells.

Apart from the above experiments on subcutaneous tumors, preliminary experiments on upconversion fluorescence imaging of intraperitoneal tumors were also carried out. The results shown in Figure S7 in the SI demonstrate that the mAb-NP probe clearly enables the visualization of tiny intraperitoneal tumors, which may shine light on the applications of the current probes in tumor surgical navigation.

Pharmacokinetic Behaviors of PEGylated $NaGdF_4$:Yb,Er Nanoparticles. For nanoprobes capable of targeting tumors *via* the specific interactions between the targeting moiety in the probes and protein receptors on the tumor cell surface, they have to first cross walls of blood vessels and then the matrix tissue surrounding the target cells driven by diffusion.[58] Although the barrier in vessels is no longer an existing barrier in tumor, reaching the target cell still requires high enough probe concentration in plasma as the driving force for continued tumor accumulation. Until now, there is still limited literature on *in vivo* imaging of tumors by using RE-based nanoprobes delivered *via* intravenous injection,[38,40,45] although various types of tumor-specific ligands were used to construct differently structured nanoprobes.[67,68] Apart from the reduced plasma residence time caused by possible agglomeration of nanoprobes, the size-dependent pharmacokinetic behaviors of differently sized nanoparticles remain to be elucidated. Even though the biodistributions of different types of inorganic nanoparticles have been increasingly studied,[39,69−71] the results are less comparable due to the differences in particle size, surface coating structure, and solution properties under physiological conditions, *etc.* Moreover, the analytical methods may also give rise to

diverse results. For example, the renal clearance of Q-dots and biodistribution of $NaYF_4$:Yb,Er nanoparticles were investigated by detecting the optical emissions of the particles,[39,69] upon the assumptions that Q-dots and RE-based nanocrystals possess stable optical emissions *in vivo* over the long run. Radioactive isotopes were also used to track the biodistributions of different types of inorganic nanoparticles.[72,73] However, the detachment of the radioactive isotopes normally bound to the particle surface *via* organic ligands may also cause errors in the results.

The excellent colloidal stability endowed by the reliable PEGylation approach mentioned above offered the opportunity to study the particle size dependent pharmacokinetic behaviors. Owing to the very low abundance of rare-earth elements in animals, ICP-AES analysis also offers an alternative but more accurate measure for studying the biodistribution of RE-based nanoparticles.

Because the minimum size of $NaGdF_4$ particles achieved by the current synthetic method is much smaller than that for $NaGdF_4$:Yb,Er particles, $NaGdF_4$ particles of 5.1 $\pm$ 0.4 nm were prepared and used to compare with the largest spherical $NaGdF_4$:Yb,Er particles (18.5 $\pm$ 1.3 nm) obtained through the current synthetic approach for showing the particle size-determined pharmacokinetic behaviors. The identical surface coordination chemistry for ligand exchange largely guarantees the comparability of these two particle samples with respect to their surface properties, so as to solely reflect the particle size effects. We did not choose $NaGdF_4$:Yb,Er particles of 24.6 $\pm$ 1.1 nm as the large particle model because they are not perfectly spherical.

As shown in Figure 9, the liver and spleen accumulations of these two particles become dominant 24 h postadministration, similar to the behaviors of $NaGdF_4$:Yb,Er particles of 24.6 $\pm$ 1.1 nm, as shown in Figure 8. However, the total uptakes by liver and spleen, determined at 24 h postinjection, are summed up to 53.4% and 87.6% for 5.1 nm particles and 18.5 nm particles, respectively. That the small particle presents lower liver concentrations (%ID/g) in comparison with the large counterpart implies that the small particle may be excreted *via* renal elimination. By fitting the blood concentrations of both particles acquired at different time points postinjection, using a monocompartment model, the blood half-time is calculated to be 178 and 66 min for the 5.1 and 18.5 nm particle, respectively, as shown in Figure 10a. The difference in blood half-time suggests that the small particle has a higher probability of being excreted through the renal elimination pathway. The results shown in Figure 9 further reveal that liver concentrations of both particles decrease with time, while spleen concentrations of both particles present generally reversed tendencies, suggesting that both of these nanoparticles may also take a biliary elimination pathway.

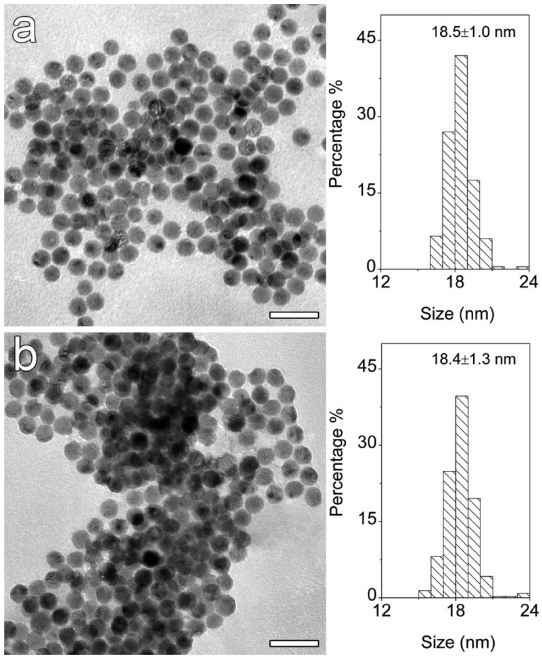

Figure 11. TEM images and particle size histograms of 18.5 nm $NaGdF_4$:Yb,Er particles found in feces collected on the 3rd day (a) and 14th day (b) postinjection. The bar corresponds to 50 nm.

To further disclose the elimination pathways, urine and feces were continuously collected and quantitatively determined. In brief, ~12% of the small particles were excreted *via* urine during the first day postinjection, followed by ~8% during the second day postinjection, while nearly no large particles were detected in urine, suggesting that renal clearance is one of the major elimination pathways for particles of 5.1 nm but not for particles of 18.5 nm. Further analysis on feces suggests that the biliary pathway was taken by both of these particle samples. As shown in Figure 10b, approximately 46% of small particles and 38% of the large particles are excreted after 7 d postadministration, which further increase to 53% and 78%, respectively, after 14 d. The fecal excretion rates of small particles and large particles eventually reach 61% and 87%, respectively, after 30 d. The biological half-time is thus estimated to be 8.2 d for 18.5 nm particles according to the fecal excretion data. Since small particles also took the renal elimination pathway, the biological half-time was estimated, according to their accumulations in main organs, as shown in Figure 9, to be 1.4 d.

To further confirm that rare-earth elements in feces remained in the form of particles, a feces sample excreted on the third day postinjection of 5.1 nm was collected, purified, and then subjected to TEM analysis. Due to the small size and the interference of fecal residue, it was hard to identify the particles. However, the electron diffraction pattern shown in Figure S8 strongly supported that the small particles excreted remain in the particle form. Further TEM results on

purified feces samples collected on the third day and 14th day postinjection of large particles are shown in Figure 11. Statistical analysis reveals that the average size of large particles found in feces is 18.5 ± 1.0 nm (3rd day) and 18.4 ± 1.3 nm (14th day), respectively. TEM results also suggest that the particles do not change in shape. According to the *t* test ($p = 0.69 > 0.05$), they do not change in size either, which helps to relieve the concerns on the toxicity of Gd^{3+} possibly released by $NaGdF_4$ particles.

In fact, the solubility of $NaGdF_4$ remains unavailable in the literature. Our preliminary experiments provided in the SI suggest that the maximum amount of Gd^{3+} ions released by $NaGdF_4$ particles in 20 mL of Milli-Q water, corresponding to the average volume of nude mice, is around 126 fmol. Since Na^+ ion is highly abundant in human beings and mice as well, the practical amount of Gd^{3+} possibly released within the body should be much lower.

CONCLUSIONS

In summary, highly monodispersed oleate-capped $NaGdF_4$:Yb,Er nanocrystals were prepared *via* replacement reactions taking place at 300 °C. Systematic experiments reveal that F^-:Ln^{3+} and Na^+:Ln^{3+} feeding ratios are effective variables for regulating the size and shape of the resultant nanocrystals. With reference to the stoichiometric ratio of Na^+:Ln^{3+}:F^- in $NaGdF_4$:Yb,Er, decreasing the F^-:Ln^{3+} ratio or increasing the Na^+:Ln^{3+} ratio favors the formation of monodispersed $NaGdF_4$:Yb,Er nanocrystals in spherical or quasi-spherical shapes. Conversely, increasing the F^-:Ln^{3+} ratio encourages repetition nucleation, resulting in a broadened size distribution, while decreasing the Na^+:Ln^{3+} ratio leads to $NaGdF_4$:Yb,Er nanosheets instead of spherical nanocrystals. In other words, properly balancing the surface coverage of F^-, Na^+, and Ln^{3+} is one of the keys to regulate the size and shape of oleate-capped $NaGdF_4$:Yb,Er nanocrystals. Accordingly, monodispersed $NaGdF_4$:Yb,Er nanocrystals with appropriate size, upconversion fluorescence intensity, and green-to-red emission ratio can be obtained. A PEG ligand with two phosphate ions can effectively replace the oleic acid ligand to endow the $NaGdF_4$:Yb,Er nanocrystals with excellent colloidal stability, while the bioconjugation reaction with tumor-specific antibodies through particle surface maleimide groups leads to ultrasensitive magnetic/upconversion fluorescent dual-modal molecular probes by which both subcutaneously transplanted tumors and intraperitoneally transplanted tumors are successfully detected by MRI and upconversion fluorescence imaging. Quite outstandingly, subcutaneous tumors as small as 1.7 mm × 1.9 mm are clearly identified through upconversion fluorescence imaging. The in-depth pharmacokinetic studies reveal that the elimination pathway is particle size dependent. The biliary elimination pathway is taken by particles of 18.5 nm, and more than 87% of the particles are excreted after 30 d postadministration, while both renal and biliary clearance pathways are taken by particles of 5.1 nm, resulting in a greatly shortened biological half-time. Most importantly, the nanoparticles do not change in size and shape after being excreted, which helps to relieve the toxicity concerns on versatile *in vivo* applications of RE-based nanoprobes.

EXPERIMENTAL SECTION

Chemicals. The following materials were purchased from Sigma-Aldrich: $GdCl_3 \cdot 6H_2O$ (450855), $YbCl_3 \cdot 6H_2O$ (337927), $ErCl_3 \cdot 6H_2O$ (259256), OA (364525), 1-octadecene (ODE, O806), ammonium fluoride (NH_4F, 216011), tris(2-carboxyethyl) phosphine hydrochloride (TCEP, C4706), MTT (M2128), pentobarbital sodium (P3761), and murine immunoglobulin G (mIgG, I5381). Analytical grade chemicals such as ethanol, cyclohexane, and tetrahydrofuran (THF) were purchased from Sinopharm Chemical Reagent Beijing, Co., Ltd. mal-PEG-dp was a customized product provided by Beijing Oneder Hightech Co. Ltd. Isoflurane (NDC 10019-360-40) was purchased from Baxter Healthcare Corporation. Human gastric cancer cell line GC7901 and human colorectal cancer cell line LS180 were obtained from the Oncology School of Peking University. Monoclonal anti-EGFR antibody (Erbitux) was purchased from Boehringer Ingelheim Pharma GmbH & Co KG.

Preparation and Characterizations of $NaGdF_4$:Yb,Er Nanoparticles. The Yb/Er-doped $NaGdF_4$ nanocrystals were prepared according to a method previously reported for $NaYF_4$ nanocrystals.[29] In a typical synthesis, $GdCl_3 \cdot 6H_2O$ (0.80 mmol), $YbCl_3 \cdot 6H_2O$ (0.18 mmol), and $ErCl_3 \cdot 6H_2O$ (0.02 mmol) were mixed with 14 mL of OA and 16 mL of ODE in a 100 mL flask. The resultant mixture was then heated to 150 °C under nitrogen protection to form a homogeneous solution. After the solution was cooled to 50 °C, 10 mL of methanol solution containing NaOH (2.5 mmol) and NH_4F (4 mmol) was slowly introduced, and the reaction system was then kept under stirring at 50 °C for 30 min. Subsequently, methanol in the system was removed by keeping the reaction system at 100 °C for 10 min under vacuum. Under atmospheric pressure, the finally formed reaction mixture was heated to 300 °C. The reactions were allowed for 1 h under nitrogen protection and then terminated by cooling the reaction mixture to room temperature. The resultant nanoparticles were precipitated by ethanol, collected by centrifugation, washed with ethanol several times, and finally redispersed in THF or cyclohexane for further experiments.

To show the impact of the reactant ratio on the size, size distribution, and phase structure of the resultant $NaGdF_4$:Yb,Er nanoparticles, in the following preparations, the feeding molar ratios of F^-:Ln^{3+} and Na^+:Ln^{3+} were tuned independently between 8:1 and 2.4:1 and between 3:1 and 0.75:1, respectively, while the feeding molar ratio among the lanthanide ions, *i.e.*, Gd^{3+}:Yb^{3+}:Er^{3+}, was fixed at 80:18:2.

TEM and HRTEM measurements were carried out with JEM-100CXII and JEOL 2010 microscopes operating at 100 and 200 kV, respectively, for characterizing the particle size, shape, and crystalline structure. The particle size was determined by counting more than 300 nanoparticles per sample. In addition, XRD measurements were carried out on a Regaku D/Max-2500 diffractometer under Cu $K\alpha_1$ radiation (λ = 1.540 56 Å) for further characterizing the phase structure of the resultant nanocrystals. The concentration of the rare earth elements in different systems was determined by using ICP-AES produced

by Jiangsu Skyray Instrument Co., Ltd. after the particles were eroded with concentrated nitric acid. The upconversion fluorescence spectra were recorded on a Cary Eclipse fluorescence spectrophotometer equipped with a 980 nm CW laser diode (2 W) serving as the excitation source.

Ligand Exchange. Approximately 10 mg of the purified nanoparticles and 100 mg of mal-PEG-dp were dissolved in 5 mL of THF. Typically, the ligand exchange reaction took place overnight at room temperature. Then, the PEGylated particles were precipitated by cyclohexane, washed with cyclohexane three times, and finally dried under vacuum at room temperature. The colloidal stability and upconversion fluorescence emissions of the PEG-coated $NaGdF_4$:Yb,Er nanoparticles in Milli-Q water and PBS buffer were monitored by using DLS and a fluorescence spectrometer with a constant excitation power density, respectively.

Magnetic Relaxivity and Cytotoxicity of PEGylated $NaGdF_4$:Yb,Er Particles. The relaxivity measurements were carried out on a 3 T clinical MRI instrument (GE Signa 3.0 T HD, Milwaukee, WI, USA). A series of aqueous solutions with different concentrations of (mal-PEG-dp)-coated $NaGdF_4$:Yb,Er particles were prepared and transferred into 1.5 mL Eppendorf tubes for longitudinal magnetic relaxivity measurements. The parameters were set as follows: echo time (TE) = 15.3 ms; repetition time (TR) = 500, 1000, 1500, 2000 ms; number of excitations (NEX) = 8.

MTT assays using human gastric carcinoma cell line GC7901 were carried out to evaluate the cytotoxicity of the PEGylated $NaGdF_4$:Yb,Er particles according to a previous report.[12]

Preparation of mAb-$NaGdF_4$:Yb,Er Probe. Typically, anti-EGFR monoclonal antibody (1 mg/mL in 10× PBS) was subjected to mild reduction by TCEP to convert the disulfide groups in the Fc fragments to thiols. The partially reduced mAb was purified by using 30-K MWCO centrifugal devices (Millipore YM-30). The EGFR-specific probe was prepared by mixing the (mal-PEG-dp)-coated $NaGdF_4$:Yb,Er particles with the partially reduced anti-EGFR mAb in Tris-buffered saline (TBS, pH 7.04). The resultant conjugate mAb-NP was transferred into 1× PBS buffer and stored at 4 °C for further use. In similar way, the reference probe mIgG-NP was prepared. The conjugation efficiency and the formation of the conjugates were investigated by a Cary Eclipse fluorescence spectrophotometer and dynamic light scattering.

Animal Tumor Models. The tumor models used were established upon intraperitoneal or subcutaneous injections of LS180 cells ($\sim 5 \times 10^6$) into 4−6-week-old male BALB/c nude mice. The tumor imaging studies were carried out 5−7 d after the inoculation of tumor cells.

MR and Upconversion Fluorescence Imaging of Tumors *in Vivo*. The dose level was set to 15 mg of Gd per kilogram body weight for PEGylated $NaGdF_4$:Yb,Er particles (NP), particle probes (mAb-NP, mIgG-NP), and Gd-DTPA in all imaging experiments.

The MR images were acquired on a 4.7 T animal MRI instrument (Bruker 4.7 T HD, Milwaukee, WI, USA) at designated time points postinjection. The detailed imaging parameters were set as follows: field of view (FOV) = 3.5 × 4.5 cm^2; matrix size = 128 × 128; slice thickness = 1 mm; echo time (TE) = 11 ms; repetition time (TR) = 90, 150, 300, 500, 800, 1200, 2000, and 3000 ms; number of excitations (NEX) = 4. T1 maps were calculated by pixel-wise fitting of the TR-dependent signal intensity changes to a single-exponential function. The mice were anesthetized by 1% isoflurane delivered *via* a nose cone during the imaging sessions.

The upconversion fluorescent images of tumors were captured using a digital camera (EOS450D, Canon) equipped with an 800 nm short-pass filter. The beam size of the CW 980 nm laser was 6 mm, larger than the tumors transplanted. The excitation light density was ~2.8 W/cm^2. The distance between the skin on top of the tumor and the laser diode was 20 mm.

Histology Study. The subcutaneous tumors were harvested and then kept in 10% formalin for 3 d. After being embedded into paraffin, the fixed tumors were sliced, stained with hematoxylin and eosin (H&E), and then subjected to microscopy study.

Pharmacokinetics of PEGylated $NaGdF_4$:Yb,Er Nanoparticles. Male, 6-week-old Kunming mice were adopted for the pharmacokinetic studies of differently sized PEG-coated particles, *i.e.*, 5.1 nm $NaGdF_4$ and 18.5 nm $NaGdF_4$:Yb,Er, after they were intravenously injected into groups of mice (n = 4). The dose level was the same as that for imaging experiments. Blood samples were obtained *via* retro-orbital blood collection at 1 min, 10 min, 30 min, 1 h, 2 h, 4 h, 8 h, 24 h, 48 h, and 72 h postinjection. The Gd content in the plasma was determined by ICP-AES after the red blood cells were removed by centrifugation at 1000 rpm. The following organs and tissues including liver, spleen, kidney, heart, lung, stomach, brain, intestine, skin, muscle, bone (hind leg), and blood were collected, weighed, dissected, and eroded with concentrated nitric acid and H_2O_2 for disclosing the biodistributions of the particles by ICP-AES at 2 h, 24 h, 3 d, 7 d, 14 d, and 30 d postinjection, respectively.

The urine and feces were continuously collected from mice (n = 8) housed in the metabolic cage and then weighed, homogenized, lyophilized, and eroded to determine the Gd contents for studying the nanoparticle clearance. In addition, the particles found in feces were also subjected to TEM observation after being isolated.

All animal experiments reported herein were carried out according to a protocol approved by Peking University Institutional Animal Care and Use Committee.

Conflict of Interest: The authors declare no competing financial interest.

Acknowledgment. The authors thank the National Basic Research Program of China (2011CB935800), NSFC (21203211, 81090271, 21003135, 21021003), and CAS (KJCX2-YW-M15) for financial support.

Supporting Information Available: (1) TEM image of the tiny nuclei formed during the nucleation process at 50 °C, (2) HRTEM and XRD results on 14.6 nm $NaGdF_4$:Yb,Er nanoparticles, (3) electron diffraction patterns of 11.5 nm spherical $NaGdF_4$:Yb,Er nanoparticles and 82.3 nm $NaGdF_4$:Yb,Er nanosheets, (4) normalized upconversion fluorescence spectra recorded from PEGylated $NaGdF_4$:Yb,Er nanoparticles in water and the oleate-coated counterparts in cyclohexane upon excitation by a 980 nm laser, (5) spectroscopy studies on the conjugation reaction between mAb and (mal-PEG-dp)-coated $NaGdF_4$:Yb,Er particles, (6) DLS investigations on the bioconjugation reaction, (7) true-color upconversion fluorescence imaging of intraperitoneal tumors, (8) electron diffraction pattern of 5.1 nm $NaGdF_4$ particles found in feces collected on the 3rd day postadministration, (9) detailed experiments evaluating the water solubility of $NaGdF_4$ nanoparticles. This material is available free of charge *via* the Internet at http://pubs.acs.org.

REFERENCES AND NOTES

1. Lee, H. Y.; Li, Z.; Chen, K.; Hsu, A. R.; Xu, C. J.; Xie, J.; Sun, S. H.; Chen, X. Y. PET/MRI Dual-Modality Tumor Imaging Using Arginine-Glycine-Aspartic (RGD) - Conjugated Radiolabeled Iron Oxide Nanoparticles. *J. Nucl. Med.* **2008**, *49*, 1371–1379.
2. Qiao, R. R.; Yang, C. H.; Gao, M. Y. Superparamagnetic Iron Oxide Nanoparticles: From Preparations to *in Vivo* MRI Applications. *J. Mater. Chem.* **2009**, *19*, 6274–6293.
3. Sun, C.; Veiseh, O.; Gunn, J.; Fang, C.; Hansen, S.; Lee, D.; Sze, R.; Ellenbogen, R. G.; Olson, J.; Zhang, M. *In Vivo* MRI Detection of Gliomas by Chlorotoxin-Conjugated Superparamagnetic Nanoprobes. *Small* **2008**, *4*, 372–379.
4. Navarro, G.; Maiwald, G.; Haase, R.; Rogach, A. L.; Wagner, E.; de Ilarduya, C. T.; Ogris, M. Low Generation Pamam Dendrimer and CPG Free Plasmids Allow Targeted and Extended Transgene Expression in Tumors after Systemic Delivery. *J. Controlled Release* **2010**, *146*, 99–105.
5. Xing, R. J.; Liu, G.; Quan, Q. M.; Bhirde, A.; Zhang, G. F.; Jin, A.; Bryant, L. H.; Zhang, A.; Liang, A.; Eden, H. S.; *et al.* Functional MnO Nanoclusters for Efficient Sirna Delivery. *Chem. Commun.* **2011**, *47*, 12152–12154.
6. Rabin, O.; Perez, J. M.; Grimm, J.; Wojtkiewicz, G.; Weissleder, R. An X-Ray Computed Tomography Imaging Agent Based on Long-Circulating Bismuth Sulphide Nanoparticles. *Nat. Mater.* **2006**, *5*, 118–122.

7. Lee, J. H.; Huh, Y. M.; Jun, Y.; Seo, J.; Jang, J.; Song, H. T.; Kim, S.; Cho, E. J.; Yoon, H. G.; Suh, J. S.; *et al*. Artificially Engineered Magnetic Nanoparticles for Ultra-Sensitive Molecular Imaging. *Nat. Med.* **2007**, *13*, 95–99.
8. Liu, S. J.; Jia, B.; Qiao, R. R.; Yang, Z.; Yu, Z. L.; Liu, Z. F.; Liu, K.; Shi, J. Y.; Han, O. Y.; Wang, F.; *et al*. A Novel Type of Dual-Modality Molecular Probe for MR and Nuclear Imaging of Tumor: Preparation, Characterization and *in Vivo* Application. *Mol. Pharmaceutics* **2009**, *6*, 1074–1082.
9. Gao, X. H.; Cui, Y. Y.; Levenson, R. M.; Chung, L. W. K.; Nie, S. M. *In Vivo* Cancer Targeting and Imaging with Semiconductor Quantum Dots. *Nat. Biotechnol.* **2004**, *22*, 969–976.
10. Bhushan, K. R.; Misra, P.; Liu, F.; Mathur, S.; Lenkinski, R. E.; Frangioni, J. V. Detection of Breast Cancer Microcalcifications Using a Dual-Modality SPECT/NIR Fluorescent Probe. *J. Am. Chem. Soc.* **2008**, *130*, 17648–17649.
11. Borden, M. A.; Zhang, H.; Gillies, R. J.; Dayton, P. A.; Ferrara, K. W. A Stimulus-Responsive Contrast Agent for Ultrasound Molecular Imaging. *Biomaterials* **2008**, *29*, 597–606.
12. Hou, Y.; Qiao, R. R.; Fang, F.; Wang, X. X.; Dong, C. Y.; Liu, K.; Liu, C. Y.; Liu, Z. F.; Lei, H.; Wang, F.; *et al*. $NaGdF_4$ Nanoparticle-Based Molecular Probes for Magnetic Resonance Imaging of Intraperitoneal Tumor Xenografts *in Vivo*. *ACS Nano* **2013**, *7*, 330–338.
13. Johnson, N. J. J.; Oakden, W.; Stanisz, G. J.; Prosser, R. S.; van Veggel, F. C. J. M. Size-Tunable, Ultrasmall $NaGdF_4$ Nanoparticles: Insights into Their T-1 MRI Contrast Enhancement. *Chem. Mater.* **2011**, *23*, 3714–3722.
14. Kumar, R.; Nyk, M.; Ohulchanskyy, T. Y.; Flask, C. A.; Prasad, P. N. Combined Optical and MR Bioimaging Using Rare Earth Ion Doped $NaYF_4$ Nanocrystals. *Adv. Funct. Mater.* **2009**, *19*, 853–859.
15. Park, Y. I.; Kim, J. H.; Lee, K. T.; Jeon, K. S.; Bin Na, H.; Yu, J. H.; Kim, H. M.; Lee, N.; Choi, S. H.; Baik, S. I.; *et al*. Nonblinking and Nonbleaching Upconverting Nanoparticles as Anoptical Imaging Nanoprobe and T1 Magnetic Resonance Imaging Contrast Agent. *Adv. Mater.* **2009**, *21*, 4467–4471.
16. He, M.; Huang, P.; Zhang, C. L.; Hu, H. Y.; Bao, C. C.; Gao, G.; He, R.; Cui, D. X. Dual Phase-Controlled Synthesis of Uniform Lanthanide-Doped $NaGdF_4$ Upconversion Nanocrystals *via* an OA/Ionic Liquid Two-Phase System for *in Vivo* Dual-Modality Imaging. *Adv. Funct. Mater.* **2011**, *21*, 4470–4477.
17. Liu, C. H.; Wang, H.; Zhang, X. R.; Chen, D. P. Morphology- and Phase-Controlled Synthesis of Monodisperse Lanthanide-Doped $NaGdF_4$ Nanocrystals with Multicolor Photoluminescence. *J. Mater. Chem.* **2009**, *19*, 489–496.
18. Zhou, J.; Sun, Y.; Du, X. X.; Xiong, L. Q.; Hu, H.; Li, F. Y. Dual-Modality *in Vivo* Imaging Using Rare-Earth Nanocrystals with Near-Infrared to Near-Infrared (NIR-to-NIR) Upconversion Luminescence and Magnetic Resonance Properties. *Biomaterials* **2010**, *31*, 3287–3295.
19. Wang, G. F.; Peng, Q.; Li, Y. D. Lanthanide-Doped Nanocrystals: Synthesis, Optical-Magnetic Properties, and Applications. *Acc. Chem. Res.* **2011**, *44*, 322–332.
20. Mai, H. X.; Zhang, Y. W.; Si, R.; Yan, Z. G.; Sun, L. D.; You, L. P.; Yan, C. H. High-Quality Sodium Rare-Earth Fluoride Nanocrystals: Controlled Synthesis and Optical Properties. *J. Am. Chem. Soc.* **2006**, *128*, 6426–6436.
21. Li, Z. Q.; Zhang, Y. Monodisperse Silica-Coated Polyvinylpyrrolidone/$NaYF_4$ Nanocrystals with Multicolor Upconversion Fluorescence Emission. *Angew. Chem., Int. Ed.* **2006**, *45*, 7732–7735.
22. Mai, H. X.; Zhang, Y. W.; Sun, L. D.; Yan, C. H. Highly Efficient Multicolor Up-conversion Emissions and Their Mechanisms of Monodisperse $NaYF_4$:Yb,Er Core and Core/Shell-Structured Nanocrystals. *J. Phys. Chem. C* **2007**, *111*, 13721–13729.
23. Bridot, J. L.; Faure, A. C.; Laurent, S.; Riviere, C.; Billotey, C.; Hiba, B.; Janier, M.; Josserand, V.; Coll, J. L.; Vander Elst, L.; *et al*. Hybrid Gadolinium Oxide Nanoparticles: Multimodal Contrast Agents for *in Vivo* Imaging. *J. Am. Chem. Soc.* **2007**, *129*, 5076–5084.
24. Stouwdam, J. W.; van Veggel, F. C. J. M. Near-Infrared Emission of Redispersible Er^{3+}, Nd^{3+}, and Ho^{3+} Doped LaF_3 Nanoparticles. *Nano Lett.* **2002**, *2*, 733–737.
25. Zhang, F.; Wan, Y.; Yu, T.; Zhang, F. Q.; Shi, Y. F.; Xie, S. H.; Li, Y. G.; Xu, L.; Tu, B.; Zhao, D. Y. Uniform Nanostructured Arrays of Sodium Rare-Earth Fluorides for Highly Efficient Multicolor Upconversion Luminescence. *Angew. Chem., Int. Ed.* **2007**, *46*, 7976–7979.
26. Cao, Y. C. Synthesis of Square Gadolinium-Oxide Nanoplates. *J. Am. Chem. Soc.* **2004**, *126*, 7456–7457.
27. Boyer, J. C.; Vetrone, F.; Cuccia, L. A.; Capobianco, J. A. Synthesis of Colloidal Upconverting $NaYF_4$ Nanocrystals Doped with Er^{3+}, Yb^{3+} and Tm^{3+}, Yb^{3+} *via* Thermal Decomposition of Lanthanide Trifluoroacetate Precursors. *J. Am. Chem. Soc.* **2006**, *128*, 7444–7445.
28. Wang, F.; Han, Y.; Lim, C. S.; Lu, Y. H.; Wang, J.; Xu, J.; Chen, H. Y.; Zhang, C.; Hong, M. H.; Liu, X. G. Simultaneous Phase and Size Control of Upconversion Nanocrystals through Lanthanide Doping. *Nature* **2010**, *463*, 1061–1065.
29. Li, Z. Q.; Zhang, Y. An Efficient and User-Friendly Method for the Synthesis of Hexagonal-Phase $NaYF_4$:Yb,Er/Tm Nanocrystals with Controllable Shape and Upconversion Fluorescence. *Nanotechnology* **2008**, *19*, 345606.
30. Rockenberger, J.; Scher, E. C.; Alivisatos, A. P. A New Nonhydrolytic Single-Precursor Approach to Surfactant-Capped Nanocrystals of Transition Metal Oxides. *J. Am. Chem. Soc.* **1999**, *121*, 11595–11596.
31. Hyeon, T.; Lee, S. S.; Park, J.; Chung, Y.; Bin Na, H. Synthesis of Highly Crystalline and Monodisperse Maghemite Nanocrystallites without a Size-Selection Process. *J. Am. Chem. Soc.* **2001**, *123*, 12798–12801.
32. Huang, W. J.; Lu, C. H.; Jiang, C. F.; Wang, W.; Song, J. B.; Ni, Y. R.; Xu, Z. Z. Controlled Synthesis of $NaYF_4$ Nanoparticles and Upconversion Properties of $NaYF_4$:Yb,Er(Tm)/Fc Transparent Nanocomposite Thin Films. *J. Colloid Interface Sci.* **2012**, *376*, 34–39.
33. Zhao, J. B.; Lu, Z. D.; Yin, Y. D.; Mcrae, C.; Piper, J. A.; Dawes, J. M.; Jin, D. Y.; Goldys, E. M. Upconversion Luminescence with Tunable Lifetime in $NaYF_4$:Yb,Er Nanocrystals: Role of Nanocrystal Size. *Nanoscale* **2013**, *5*, 944–952.
34. Shi, F.; Wang, J. S.; Zhang, D. S.; Qin, G. S.; Qin, W. P. Greatly Enhanced Size-Tunable Ultraviolet Upconversion Luminescence of Monodisperse Beta-$NaYF_4$:Yb,Tm Nanocrystals. *J. Mater. Chem.* **2011**, *21*, 13413–13421.
35. Bao, L. Y.; Li, Z. Q.; Tao, Q. L.; Xie, J. J.; Mei, Y. Y.; Xiong, Y. J. Controlled Synthesis of Uniform LaF_3 Polyhedrons, Nanorods and Nanoplates Using NaOH and Ligands. *Nanotechnology* **2013**, *24*, 145604.
36. Zhou, J.; Yu, M. X.; Sun, Y.; Zhang, X. Z.; Zhu, X. J.; Wu, Z. H.; Wu, D. M.; Li, F. Y. Fluorine-18-Labeled Gd^{3+}/Yb^{3+}/Er^{3+} Co-Doped $NaYF_4$ Nanophosphors for Multimodality PET/MR/UCL Imaging. *Biomaterials* **2011**, *32*, 1148–1156.
37. Xia, A.; Chen, M.; Gao, Y.; Wu, D. M.; Feng, W.; Li, F. Y. Gd^{3+} Complex-Modified $NaLuF_4$-Based Upconversion Nanophosphors for Trimodality Imaging of NIR-to-NIR Upconversion Luminescence, X-Ray Computed Tomography and Magnetic Resonance. *Biomaterials* **2012**, *33*, 5394–5405.
38. Xiong, L. Q.; Chen, Z. G.; Tian, Q. W.; Cao, T. Y.; Xu, C. J.; Li, F. Y. High Contrast Upconversion Luminescence Targeted Imaging *in Vivo* Using Peptide-Labeled Nanophosphors. *Anal. Chem.* **2009**, *81*, 8687–8694.
39. Xiong, L. Q.; Yang, T. S.; Yang, Y.; Xu, C. J.; Li, F. Y. Long-Term *in Vivo* Biodistribution Imaging and Toxicity of Polyacrylic Acid-Coated Upconversion Nanophosphors. *Biomaterials* **2010**, *31*, 7078–7085.
40. Park, Y.; Kim, H. M.; Kim, J. H.; Moon, K. C.; Yoo, B.; Lee, K. T.; Lee, N.; Choi, Y.; Park, W.; Ling, D.; *et al*. Theranostic Probe Based on Lanthanide-Doped Nanoparticles for Simultaneous *in Vivo* Dual-Modal Imaging and Photodynamic Therapy. *Adv. Mater.* **2012**, *24*, 5755–5761.
41. Fan, W.; Shen, B.; Bu, W.; Chen, F.; Zhao, K.; Zhang, S.; Zhou, L.; Peng, W.; Xiao, Q.; Xing, H.; *et al*. Rattle-Structured Multifunctional Nanotheranostics for Synergetic Chemo-/Radiotherapy and Simultaneous Magnetic/Luminescent Dual-Mode Imaging. *J. Am. Chem. Soc.* **2013**, *135*, 6494–6503.

42. Xing, H. Y.; Bu, W. B.; Zhang, S. J.; Zheng, X. P.; Li, M.; Chen, F.; He, Q. J.; Zhou, L. P.; Peng, W. J.; Hua, Y. Q.; *et al*. Multifunctional Nanoprobes for Upconversion Fluorescence, MR and CT Trimodal Imaging. *Biomaterials* **2012**, *33*, 1079–1089.
43. Cheng, L.; Yang, K.; Li, Y. G.; Chen, J. H.; Wang, C.; Shao, M. W.; Lee, S. T.; Liu, Z. Facile Preparation of Multifunctional Upconversion Nanoprobes for Multimodal Imaging and Dual-Targeted Photothermal Therapy. *Angew. Chem., Int. Ed.* **2011**, *50*, 7385–7390.
44. Zhu, X. J.; Zhou, J.; Chen, M.; Shi, M.; Feng, W.; Li, F. Y. Core-Shell Fe_3O_4@$NaLuF_4$:Yb,Er/Tm Nanostructure for MRI, CT and Upconversion Luminescence Tri-Modality Imaging. *Biomaterials* **2012**, *33*, 4618–4627.
45. Lee, J.; Lee, T. S.; Ryu, J.; Hong, S.; Kang, M.; Im, K.; Kang, J. H.; Lim, S. M.; Park, S.; Song, R. RGD Peptide-Conjugated Multimodal $NaGdF_4$:Yb^{3+}/Er^{3+} Nanophosphors for Upconversion Luminescence, MR, and PET Imaging of Tumor Angiogenesis. *J. Nucl. Med.* **2013**, *54*, 96–103.
46. Yang, L. L.; Mao, H.; Wang, Y. A.; Cao, Z. H.; Peng, X. H.; Wang, X. X.; Duan, H. W.; Ni, C. C.; Yuan, Q. G.; Adams, G.; *et al*. Single Chain Epidermal Growth Factor Receptor Antibody Conjugated Nanoparticles for *in Vivo* Tumor Targeting and Imaging. *Small* **2009**, *5*, 235–243.
47. Yang, L.; Mao, H.; Cao, Z. H.; Wang, Y. A.; Peng, X. H.; Wang, X. X.; Sajja, H. K.; Wang, L. Y.; Duan, H. W.; Ni, C. C.; *et al*. Molecular Imaging of Pancreatic Cancer in an Animal Model Using Targeted Multifunctional Nanoparticles. *Gastroenterology* **2009**, *136*, 1514–1525.
48. Naito, S.; Voneschenbach, A. C.; Giavazzi, R.; Fidler, I. J. Growth and Metastasis of Tumor-Cells Isolated from a Human Renal-Cell Carcinoma Implanted into Different Organs of Nude-Mice. *Cancer Res.* **1986**, *46*, 4109–4115.
49. Hendriksen, E. M.; Span, P. N.; Schuuring, J.; Peters, J. P. W.; Sweep, F. C. G. J.; van der Kogel, A. J.; Bussink, J. Angiogenesis, Hypoxia and VEGF Expression during Tumour Growth in a Human Xenograft Tumour Model. *Microvasc. Res.* **2009**, *77*, 96–103.
50. Xiao, K.; Luo, J. T.; Li, Y. P.; Xiao, W. W.; Lee, J. S.; Gonik, A. M.; Lam, K. S. The Passive Targeting of Polymeric Micelles in Various Types and Sizes of Tumor Models. *Nanosci. Nanotechnol. Lett.* **2010**, *2*, 79–85.
51. Duncan, R.; Sat, Y. N. Tumour Targeting by Enhanced Permeability and Retention (EPR) Effect. *Ann. Oncol.* **1998**, *9*, 39–39.
52. Sevick, E. M.; Jain, R. K. Geometric Resistance to Blood-Flow in Solid Tumors Perfused Exvivo - Effects of Tumor Size and Perfusion-Pressure. *Cancer Res.* **1989**, *49*, 3506–3512.
53. Hu, F. Q.; Wei, L.; Zhou, Z.; Ran, Y. L.; Li, Z.; Gao, M. Y. Preparation of Biocompatible Magnetite Nanocrystals for *in Vivo* Magnetic Resonance Detection of Cancer. *Adv. Mater.* **2006**, *18*, 2553–2556.
54. Chen, M.; Wu, B. H.; Yang, J.; Zheng, N. F. Small Adsorbate-Assisted Shape Control of Pd and Pt Nanocrystals. *Adv. Mater.* **2012**, *24*, 862–879.
55. Shan, J. N.; Ju, Y. G. A Single-Step Synthesis and the Kinetic Mechanism for Monodisperse and Hexagonal-Phase $NaYF_4$:Yb, Er Upconversion Nanophosphors. *Nanotechnology* **2009**, *20*, 275603.
56. Wang, F.; Wang, J. A.; Liu, X. G. Direct Evidence of a Surface Quenching Effect on Size-Dependent Luminescence of Upconversion Nanoparticles. *Angew. Chem., Int. Ed.* **2010**, *49*, 7456–7460.
57. Nie, S. M. Understanding and Overcoming Major Barriers in Cancer Nanomedicine. *Nanomedicine* **2010**, *5*, 523–528.
58. Fang, J.; Nakamura, H.; Maeda, H. The EPR Effect: Unique Features of Tumor Blood Vessels for Drug Delivery, Factors Involved, and Limitations and Augmentation of the Effect. *Adv. Drug Delivery Rev.* **2011**, *63*, 136–151.
59. Pellegrino, T.; Manna, L.; Kudera, S.; Liedl, T.; Koktysh, D.; Rogach, A. L.; Keller, S.; Radler, J.; Natile, G.; Parak, W. J. Hydrophobic Nanocrystals Coated with an Amphiphilic Polymer Shell: A General Route to Water Soluble Nanocrystals. *Nano Lett.* **2004**, *4*, 703–707.
60. Robinson, D. B.; Persson, H. H. J.; Zeng, H.; Li, G. X.; Pourmand, N.; Sun, S. H.; Wang, S. X. DNA-Functionalized MFe_2O_4 (M = Fe, Co, or Mn) Nanoparticles and Their Hybridization to DNA-Functionalized Surfaces. *Langmuir* **2005**, *21*, 3096–3103.
61. Xie, J.; Xu, C.; Kohler, N.; Hou, Y.; Sun, S. Controlled Pegylation of Monodisperse Fe_3O_4 Nanoparticles for Reduced Non-Specific Uptake by Macrophage Cells. *Adv. Mater.* **2007**, *19*, 3163–3166.
62. Huh, Y. M.; Jun, Y. W.; Song, H. T.; Kim, S.; Choi, J. S.; Lee, J. H.; Yoon, S.; Kim, K. S.; Shin, J. S.; Suh, J. S.; *et al*. *In Vivo* Magnetic Resonance Detection of Cancer by Using Multifunctional Magnetic Nanocrystals. *J. Am. Chem. Soc.* **2005**, *127*, 12387–12391.
63. Wang, L. Y.; Yan, R. X.; Hao, Z. Y.; Wang, L.; Zeng, J. H.; Bao, H.; Wang, X.; Peng, Q.; Li, Y. D. Fluorescence Resonant Energy Transfer Biosensor Based on Upconversion-Luminescent Nanoparticles. *Angew. Chem., Int. Ed.* **2005**, *44*, 6054–6057.
64. Yi, G. S.; Chow, G. M. Water-Soluble $NaYF_4$:Yb,Er(Tm)/$NaYF_4$/Polymer Core/Shell/Shell Nanoparticles with Significant Enhancement of Upconversion Fluorescence. *Chem. Mater.* **2007**, *19*, 341–343.
65. Boyer, J. C.; Manseau, M. P.; Murray, J. I.; van Veggel, F. C. J. M. Surface Modification of Upconverting $NaYF_4$ Nanoparticles with PEG-Phosphate Ligands for NIR (800 nm) Biolabeling within the Biological Window. *Langmuir* **2010**, *26*, 1157–1164.
66. Sun, C.; Lee, J. S. H.; Zhang, M. Q. Magnetic Nanoparticles in MR Imaging and Drug Delivery. *Adv. Drug Delivery Rev.* **2008**, *60*, 1252–1265.
67. Ju, Q.; Tu, D. T.; Liu, Y. S.; Li, R. F.; Zhu, H. M.; Chen, J. C.; Chen, Z.; Huang, M. D.; Chen, X. Y. Amine-Functionalized Lanthanide-Doped $KGdF_4$ Nanocrystals as Potential Optical/Magnetic Multimodal Bioprobes. *J. Am. Chem. Soc.* **2012**, *134*, 1323–1330.
68. Bogdan, N.; Rodriguez, E. M.; Sanz-Rodriguez, F.; de la Cruz, M. C. I.; Juarranz, A.; Jaque, D.; Sole, J. G.; Capobianco, J. A. Bio-Functionalization of Ligand-Free Upconverting Lanthanide Doped Nanoparticles for Bio-Imaging and Cell Targeting. *Nanoscale* **2012**, *4*, 3647–3650.
69. Choi, H. S.; Liu, W.; Misra, P.; Tanaka, E.; Zimmer, J. P.; Ipe, B. I.; Bawendi, M. G.; Frangioni, J. V. Renal Clearance of Quantum Dots. *Nat. Biotechnol.* **2007**, *25*, 1165–1170.
70. Hong, G. S.; Robinson, J. T.; Zhang, Y. J.; Diao, S.; Antaris, A. L.; Wang, Q. B.; Dai, H. J. *In Vivo* Fluorescence Imaging with Ag_2S Quantum Dots in the Second near-Infrared Region. *Angew. Chem., Int. Ed.* **2012**, *51*, 9818–9821.
71. Lipka, J.; Semmler-Behnke, M.; Sperling, R. A.; Wenk, A.; Takenaka, S.; Schleh, C.; Kissel, T.; Parak, W. J.; Kreyline, W. G. Biodistribution of PEG-Modified Gold Nanoparticles Following Intratracheal Instillation and Intravenous Injection. *Biomaterials* **2010**, *31*, 6574–6581.
72. Kryza, D.; Taleb, J.; Janier, M.; Marmuse, L.; Miladi, I.; Bonazza, P.; Louis, C.; Perriat, P.; Roux, S.; Tillement, O.; *et al*. Biodistribution Study of Nanometric Hybrid Gadolinium Oxide Particles as a Multimodal SPECT/MR/Optical Imaging and Theragnostic Agent. *Bioconjugate Chem.* **2011**, *22*, 1145–1152.
73. Ohno, K.; Akashi, T.; Tsujii, Y.; Yamamoto, M.; Tabata, Y. Blood Clearance and Biodistribution of Polymer Brush-Afforded Silica Particles Prepared by Surface-Initiated Living Radical Polymerization. *Biomacromolecules* **2012**, *13*, 927–936.